Aerofoil profile and sweep optimisation for a blended wing-body aircraft using a discrete adjoint method

A. Le Moigne and N. Qin
Department of Mechanical Engineering
University of Sheffield
Sheffield, UK

ABSTRACT

Aerodynamic optimisations of a blended wing-body (BWB) aircraft are presented. A discrete adjoint solver is used to calculate efficiently the gradients, which makes it possible to optimise for a large number of design variables. The optimisations employ either a variable-fidelity method that combines low- and high-fidelity models or a direct sequential quadratic programming (SQP) method. Four Euler optimisations of a BWB aircraft are then presented. The optimisation is allowed to change a series of master sections defining the aircraft geometry as well as the sweep angle on the outer wing for two of the optimisations. Substantial improvements are obtained, not only in the Euler mode but also when the optimised geometries are evaluated using Reynolds-averaged Navier-Stokes solutions. Some interesting features of the optimised wing profiles are discussed.

NOMENCLATURE

arc	non-dimensional arc length in the volume grid update
$B_{k,N}$	Bernstein polynomial
$\bar{c}$	mean chord
c	local chord
C_D	drag coefficient
C_L	lift coefficient
C_m	pitching moment coefficient
C_p	pressure coefficient
F	objective function
g_i	inequality constraint
$\mathbf{H}$	Hessian matrix
h_j	equality constraint
L_l	distance between two successive grid points in the volume grid update
NDV	number of design variables
$\mathbf{P}$	vector of primitive variables = $(\rho, u, v, w, p)^t$
$P_{y\,k}$	y co-ordinate of a Bézier control point
$\mathbf{Q}$	vector of conservative variables = $(\rho, \rho u, \rho v, \rho w, \rho E)^t$
$\mathbf{R}$	residual vector
$\mathbf{s}$	vector of variables in the simplified optimisation problem
t	time
u	normalised computational arc-length along a curve
V	internal volume
$\mathbf{X}$	vector of grid points
x, y, z	Cartesian co-ordinates
$\boldsymbol{\beta}$	vector of design variables = $(\beta_1, \beta_2, ..., \beta_{NDV})^t$
$\mathcal{B}$	coefficient in the beta-correction technique of the variable-fidelity method
$\mathcal{B}_q$	linear approximation of $\mathcal{B}$
$\bar{\delta}$	coefficient in the sequential quadratic programming method
Δ	increment
δ_i	coefficients in the sequential quadratic programming method

Paper No. 3083. Manuscript received 24 March 2006, accepted 31 May 2006.

https://doi.org/10.1017/S0001924000001457 Published online by Cambridge University Press

Δ_q bound on the radius of the trust-region at iteration q in the variable-fidelity method
δ_y shape increment in the y direction
η non-dimensional spanwise position
λ adjoint vector = $(\lambda_1, \lambda_2, \lambda_3, \lambda_4, \lambda_5)^t$ in 3-D
Φ_{hi} merit function in the variable-fidelity method

Subscripts

hi high-fidelity model
lo low-fidelity model
surface on the surface of the aerofoil or wing

Superscripts

* converged flow solution
l lower bound
t transpose operator
u upper bound
~ approximate Jacobian
~ indicates a corrected model in the variable-fidelity method

1.0 INTRODUCTION

The blended wing-body (BWB) aircraft is a concept for future aircraft that promises revolutionary improvements. Aerodynamically, integrating the fuselage and the wing into a large lifting surface could dramatically reduce the wetted surface to volume ratio and therefore potentially increase the lift to drag ratio, making it a greener airplane. Also a careful engine integration on the upper surface at the back of the aircraft could make it a quieter airplane. Work on this conceptual aircraft began in the 1990s in the US, involving Boeing, NASA and several universities[1-3]. The interest for this configuration then spread across the world with studies in the UK[4], Japan[5] and Russia[6]. Studies of this concept of aircraft are also reflected in some recent European projects such as MOB[7] (a computational design engine incorporating multidisciplinary design and optimisation for blended wing body configuration) and VELA[8,9] (very efficient large aircraft).

Aerodynamic optimisation on its own is a domain gaining some importance in the aeronautical industry, becoming a useful tool for aerodynamic design of wings and aircraft. A popular choice to perform such task is to use a gradient-based optimiser along with an adjoint solver, coupled to an existing CFD flow solver, to calculate efficiently and accurately the required sensitivity derivatives. Jameson[10] was the first to popularise this technique with his continuous adjoint method[11-13]. An alternative method was proposed later, where the flow equations are first discretised and then differentiated, known as the discrete adjoint formulation[14-19]. This latter method[20,21] is employed in this work for the optimisation of a BWB.

Until recently publications on aerodynamic optimisation applied to a BWB were limited to conceptual design[22,23], including at high subsonic Mach numbers[24]. Lately full three-dimensional shape optimisations at a higher level of fidelity (full potential + viscous inviscid Interaction up to Euler + viscous inviscid Interaction) have been published[8,9,25,26]. However these optimisations use finite difference to compute the function gradients when they are needed. This approach can only be applied to a small number of design variables and/or with 'cheap-to-run' aerodynamic models (low-fidelity or coarse grids) due to the computational cost associated.

In this article full three-dimensional aerodynamic optimisations of a BWB aircraft with a few hundreds of design variables are presented. This is achieved by using a discrete adjoint solver[20,21] to compute efficiently the gradients. To the authors' knowledge, this is the first publication of three-dimensional BWB optimisations using an adjoint method. This allows a great freedom in the choice of the design variables. The present optimisations are free to modify the shape and twist of some master aerofoil sections in addition to the sweep angle of the outer wing. This is also the first study that includes some sweep angle change in a three-dimensional optimisation of a BWB. Two optimisation methods are employed: a direct sequential quadratic programming (SQP) method and a variable-fidelity method[21,27-29]. Attention is paid to the longitudinal trim of the BWB, which is a critical problem for such a tailless aircraft, by including a constraint on pitching moment in the optimisations.

This article is the continuation of our earlier work carried out as part of the MOB project both on the aerodynamics of a BWB aircraft[30] and on the development of an adjoint method for optimisation[20,21]. In Ref. 31, we performed a twist redesign of the BWB and studied different spanwise lift distributions. In Ref. 32, a broader aerodynamic analysis and design were carried out, including some two-dimensional wing section optimisations, the analysis of those optimised sections when put back into the three-dimensional geometry and some preliminary three-dimensional optimisations. In this previous work, the planform was kept fixed from the conceptual design[33]. In this article, more details about the three-dimensional BWB optimisations are given and we introduce an important planform parameter, the outer wing sweep, in the design optimisation. Since the wing sweep is a key transonic design parameter, it is expected that the BWB design can be substantially improved by adding this parameter.

The current paper is arranged in the following order. First, we briefly present the CFD flow solver and the adjoint solver used in the optimisation process. The shape parameterisation and grid deformation technique are then described before detailing the two optimisation methods employed. Two optimisations of a BWB are then presented where only the aerofoil shape and twist angle are allowed to change. Finally two more BWB optimisations are detailed where in addition to the previous shape and twist changes, the sweep angle on the outer wing is introduced as a design parameter. The results are analysed regarding transonic performance of the optimised geometries.

2.0 FLOW AND ADJOINT SOLVERS

The governing equations are the three-dimensional Reynolds-averaged Navier-Stokes equations discretised in space using a cell-centred finite-volume formulation on structured multiblock grids. The convective flux calculation follows Osher's approximate Riemann solver[34,35] with a MUSCL scheme[36,37] for higher order accuracy while the viscous fluxes are calculated using central differencing. The algebraic turbulence model of Baldwin-Lomax[38] is employed for turbulent flows. The use of this simple turbulence model is justified since large separation should not feature in well-designed geometries. The boundary conditions are applied through the use of two layers of halo cells.

The temporal discretisation follows an implicit formulation[39]. After linearising the residual $\mathbf{R}$, the equations to solve iteratively are

$$\left[\frac{1}{\Delta t}\frac{\partial \mathbf{Q}}{\partial \mathbf{P}} + \frac{\partial \tilde{\mathbf{R}}(\mathbf{Q}^n)}{\partial \mathbf{P}}\right]^n \Delta \mathbf{P} = -\mathbf{R}(\mathbf{Q}^n) \quad \ldots (1)$$

with

$$\mathbf{P}^{n+1} = \mathbf{P}^n + {}^n\Delta \mathbf{P} \quad \ldots (2)$$

Note that these equations are solved for primitive variables $\mathbf{P}$ rather than conservative ones $\mathbf{Q}$. Local time-stepping is employed and the left-hand side (LHS) Jacobian of Equation (1) is approximate: it is only first-order accurate in space for the convective fluxes resulting in a seven block-diagonal matrix in 3D[40,41]. For simplicity, this structure is maintained for the diffusive terms at the cost of further approximations.

https://doi.org/10.1017/S0001924000001457 Published online by Cambridge University Press

The linearisation of the turbulent viscosity is also neglected. Despite these approximations, the boundary conditions are accurately linearised. Equation (1) is solved approximately using the block incomplete lower-upper decomposition with no fill-in or BILU(0).

The discrete adjoint equations are employed to calculate efficiently the sensitivity derivatives of the objective function F. When the adjoint vector λ satisfies the adjoint equation

$$\left(\frac{\partial \mathbf{R}}{\partial \mathbf{P}}\right)^t \lambda = -\frac{\partial F}{\partial \mathbf{P}} \quad \ldots (3)$$

the sensitivity derivatives are calculated as

$$\frac{\mathrm{d}F}{\mathrm{d}\beta_k} = \left(\frac{\partial F}{\partial \mathbf{X}}\right)^t \frac{\mathrm{d}\mathbf{X}}{\mathrm{d}\beta_k} + \lambda^t \frac{\partial \mathbf{R}}{\partial \mathbf{X}} \frac{\mathrm{d}\mathbf{X}}{\mathrm{d}\beta_k} \quad \ldots (4)$$

To solve the adjoint Equation (3), it is rewritten in the incremental iterative form[42-44] with the addition of a fictitious time term

$$\left[\frac{1}{\Delta t}\frac{\partial \mathbf{Q}}{\partial \mathbf{P}} + \frac{\partial \tilde{\mathbf{R}}(\mathbf{Q}^*)}{\partial \mathbf{P}}\bigg|^t\right]{}^n\Delta\lambda = -\left\{\frac{\partial F}{\partial \mathbf{P}} + \left[\frac{\partial \mathbf{R}(\mathbf{Q}^*)}{\partial \mathbf{P}}\bigg|^t\right]\lambda^n\right\} \quad \ldots (5)$$

with

$$\lambda^{n+1} = \lambda^n + {}^n\Delta\lambda \quad \ldots (6)$$

In this way the LHS of Equation (5) is the same as in Equation (1), before transposition. To solve Equation (5), the same BILU(0) as for the flow equations is employed for simplicity. Equation (5) is solved iteratively until convergence.

Although approximations are allowed for the LHS Jacobian of Equation (5), the right-hand side (RHS) Jacobian has to be accurate. Note that this implies a full rather than sparse matrix on the RHS due to the full stencil of the algebraic turbulence modelling. To store such a large and dense matrix would require a very large computer memory. To avoid this, the full Jacobian is not stored but each of its elements is calculated at every iteration and is multiplied by the corresponding component of the adjoint vector. This prevents a memory problem but it is at the cost of recalculating the terms constituting the Jacobian at every iteration and thus impacts on the overall computing time. (See Refs 20 and 21 for further details about the derivation of the adjoint equations and the construction of the adjoint solver which are not detailed here.)

Equation (4) is easily evaluated once the adjoint vector is known. Its terms are calculated by applying the chain rule of differentiation to the flow solver routines that compute the residual and the objective function. In the present case, these routines have been hand-differentiated.

3.0 SURFACE PARAMETERISATION

A Bézier-Bernstein parameterisation is employed to represent the shape to be modified by the optimisation process. The parameterisation is applied to a perturbation that is added to the original shape. For a two-dimensional aerofoil, deformations are limited to the vertical coordinates y

$$y_{current} = y_{initial} + \delta y \quad \ldots (7)$$

where

$$\delta y = \sum_{k=0}^{N} B_{k,N}(u) P_{yk} \quad \ldots (8)$$

with the Bernstein polynomials

$$B_{k,N}(u) = \frac{N!}{k!(N-k)!} u^k (1-u)^{N-k} \quad \ldots (9)$$

The design variables are the coefficients $P_{y\,k}$. The normalised arc-length u is rather arbitrary for deformations in only one direction. It is taken as[17]

$$u = \sqrt{x} \quad \ldots (10)$$

where x is the non-dimensionalised chordwise position of the point of ordinate $y_{initial}$. This choice for u concentrates design changes to the leading edge region of the aerofoil where x is small.

This parameterisation is applied independently to the upper and lower surface curves of the aerofoil while the leading and trailing edge points are kept fixed. An additional design variable controls the change in angle of incidence of the whole section. This parameterisation is extended to three dimensions to represent a wing shape: the wing is divided into a series of master sections that are connected linearly or using a cubic spline, each of these sections being free to deform according to the two-dimensional parameterisation presented above. The change in angle of incidence of each master section now refers to twist while for the sweep optimisations, an additional design variable controls the increment in sweep angle and moves the sections horizontally in a staggered way.

Each time the geometry is modified, the CFD grid around it has to be changed. This is performed through an analytical grid deformation technique[18,19] that propagates smoothly the geometry change through the volume grid. An original grid provides the grid point distribution along grid lines normal to the geometry, this distribution being kept in the deformed grid.

$$x_j^{new} = x_j^{original} + [1 - arc(j)]\left(x_{surface}^{new} - x_{surface}^{original}\right) \quad \ldots (11)$$

where

$$arc(j) = \frac{\sum_{l=2}^{j} L_l}{\sum_{l=2}^{jn} L_l} \quad \ldots (12)$$

$$L_l = \sqrt{(x_l - x_{l-1})^2 + (y_l - y_{l-1})^2 + (z_l - z_{l-1})^2} \quad \ldots (13)$$

and $x_{surface} = x_1$ and the point at the farfield boundary is x_{jn}. A similar transformation is done for the y and z co-ordinates. This grid deformation technique is differentiated to provide the grid sensitivities $\mathrm{d}\mathbf{X}/\mathrm{d}\beta_k$ needed in Equation (4).

4.0 OPTIMISATION TECHNIQUES

Two methods of optimisation are used in this work: a direct high-fidelity SQP optimisation and a variable-fidelity method.

4.1 Direct SQP optimisation

Let us consider the following standard optimisation problem[45,46]:

$$\begin{array}{lll} \text{Minimise } F(\beta) & & \text{objective function} \\ \text{Subject to: } g_i(\beta) \le 0 & i = 1, l & \text{inequality constraints} \\ h_j(\beta) = 0 & j = 1, m & \text{equality constraints} \\ \beta_k^l \le \beta_k \le \beta_k^u & k = 1, \mathrm{NDV} & \text{side constraints} \end{array} \quad \ldots (14)$$

Sequential quadratic programming is an optimisation technique where the search direction s is found by solving a succession of optimisation subproblems with a quadratic approximation of the original objective function and a linear approximation of the constraints. The subproblem that needs to be solved successively is

https://doi.org/10.1017/S0001924000001457 Published online by Cambridge University Press

$$\text{Minimise } \tilde{F}(\mathbf{s}) = F(\boldsymbol{\beta}^q) + \nabla F(\boldsymbol{\beta}^q)^t \mathbf{s} + \tfrac{1}{2}\mathbf{s}^t \mathbf{H}^q \mathbf{s}$$

$$\text{Subject to: } \nabla g_i(\boldsymbol{\beta}^q)^t \mathbf{s} + \delta_i g_i(\boldsymbol{\beta}^q) \le 0 \quad i = 1,l \qquad \ldots (15)$$

$$\nabla h_j(\boldsymbol{\beta}^q)^t \mathbf{s} + \bar{\delta} h_j \boldsymbol{\beta}^q) = 0 \quad j = 1,m$$

with reference to the original problem (14). Here the design variables are the components of **s** and the optimum is the search direction $\mathbf{s}^q$. The matrix $\mathbf{H}^q$ is a positive definite matrix which is initially the identity matrix and is updated during the optimisation to approximate the Hessian matrix of the Lagrangian function of problem (14). The parameters δ_i and $\bar{\delta}$, both in the interval [0,1], are used to prevent the linearisation of the constraints from creating an inconsistent problem.

Contrary to problem (14), problem (15) is a well-posed problem with a quadratic objective function and linear constraints, known as a quadratic programming problem and very efficient methods exist to solve it[45].

The SQP algorithm employed in the direct optimisations of this work is FFSQP[47]. It is a feasible SQP algorithm, which means that the designs always satisfy the constraints during the optimisation process.

4.2 Variable-fidelity method

A variable-fidelity method is the other optimisation method employed. It is based on the work of Alexandrov *et al*[27-29] where it is known as approximation model management framework (AMMF). Our own version of the method has been presented in Ref. 21 where more details are given than in this article.

Because performing optimisation directly using a high-fidelity model can be very expensive, especially for three-dimensional Navier-Stokes optimisations, this method does most of the optimisation using a 'cheap-to-run' low-fidelity model while still checking the quality of the optimisation by doing a few high-fidelity analyses. The variable-fidelity method relies on two concepts: a corrected low-fidelity model and the trust-region. The low-fidelity model is 'corrected' to mimic the high-fidelity model at certain design points. This correction is re-evaluated at the start of each low-fidelity optimisation by performing high-fidelity analysis and gradient calculations. The trust-region concept limits the validity of this corrected low-fidelity model to a region of the design space where the low-fidelity optimisation can be carried out. Its extent is also re-evaluated by comparing the performance of the low- and high-fidelity models.

Let us assume that we have a high-fidelity model F_{hi} that is to be minimised and a low-fidelity model F_{lo}. At each iteration q, the corrected low-fidelity model $\tilde{F}_{lo}$ that is used in the optimisation is required to satisfy first-order consistency with the high-fidelity model, i.e.

$$\begin{aligned} \tilde{F}_{lo}(\boldsymbol{\beta}^q) &= F_{hi}(\boldsymbol{\beta}^q) \\ \nabla\tilde{F}_{lo}(\boldsymbol{\beta}^q) &= \nabla F_{hi}(\boldsymbol{\beta}^q) \end{aligned} \qquad \ldots (16)$$

This ensures that the corrected low-fidelity model $\tilde{F}_{lo}$ behaves like F_{hi} in the neighbourhood of $\boldsymbol{\beta}^q$. Alexandrov *et al* used a beta-correction technique to construct $\tilde{F}_{lo}$ with

$$\tilde{F}_{lo}(\boldsymbol{\beta}) = \mathcal{B}_q(\boldsymbol{\beta}) F_{lo}(\boldsymbol{\beta}) \qquad \ldots (17)$$

where $\mathcal{B}_q$ is the linear approximation

$$\beta_q(\beta) = \beta(\beta^q) + \nabla\beta(\beta^q)^t(\beta - \beta^q) \qquad \ldots (18)$$

of $\mathcal{B}$ defined as;

$$\mathcal{B}(\boldsymbol{\beta}) = \frac{F_{hi}(\boldsymbol{\beta})}{F_{lo}(\boldsymbol{\beta})} \qquad \ldots (19)$$

around the point $\boldsymbol{\beta}^q$. It is easy to check that such a corrected model satisfies the requirements of Equation (16).

In the variable-fidelity method, the high-fidelity optimisation problem (14) is solved by solving a series of simplified low-fidelity optimisations of the form:

$$\text{Minimise}_{\mathbf{s}} \ \tilde{F}_{lo}(\boldsymbol{\beta}^q + \mathbf{s})$$

Subject to:

$$\begin{aligned} &\tilde{g}_{ilo}(\boldsymbol{\beta}^q) + \nabla\tilde{g}_{ilo}(\boldsymbol{\beta}^q)^t \mathbf{s} \le 0 && i = 1,l \\ &\tilde{h}_{jlo}(\boldsymbol{\beta}^q) + \nabla\tilde{h}_{jlo}(\boldsymbol{\beta}^q)^t \mathbf{s} = 0 && j = 1,m \qquad \ldots (20) \\ &\beta_k^l \le \beta_k^q + s_k \le \beta_k^u && k = 1, \text{NDV} \\ &\|\mathbf{s}\| \le \Delta_q \end{aligned}$$

where, like in the SQP method (15), the constraints have been linearised. The constraint on the norm of **s** is the result of the trust-region method that limits the application of the corrected low-fidelity models to the neighbourhood of $\boldsymbol{\beta}^q$.

FFSQP[47] is used to perform the low-fidelity optimisation of Equation (20). The fact that it is a feasible algorithm is needed here to satisfy the trust-region concept (constraint on the norm of **s**).

The variable-fidelity method is in fact very similar to a direct SQP method but instead of approximating the high-fidelity model by a quadratic function, the variable-fidelity method approximates it by a corrected low-fidelity model. The quadratic approximation is only a mathematical model while the corrected low-fidelity model is supposed to contain some physical knowledge that makes it behave like the high-fidelity model and hence the variable-fidelity method should be better than a direct SQP method if the low-fidelity model is fast enough. (The intent of this paper is not however to compare the performance of the two methods).

5.0 OPTIMISATION OF A BLENDED WING-BODY AIRCRAFT

5.1 Optimisation of the ONERA M6 Wing

A Navier-Stokes optimisation of the ONERA M6 wing[48] using the variable-fidelity method has been carried out to assess the capability of the optimisation process before applying it to a blended wing-body aircraft. This is a good test case for three-dimensional optimisation and similar optimisations of the M6 wing can be found in the literature for viscous turbulent flows[16,49-51]. The results of this optimisation have already been presented in Ref. 21. Here we only give the key elements.

The test case selected is the standard one at 3·06° of incidence with a Mach number of 0·84 and a Reynolds number of $11{\cdot}7 \times 10^6$ based on the mean aerodynamic chord. The aim of the optimisation is to reduce drag while maintaining the lift coefficient obtained at these conditions and satisfying a constraint on the interior surface of 6 wing sections. The wing is indeed divided into six master sections connected linearly in the spanwise direction. In total 86 design variables control the shape and twist of these master sections. The low-fidelity model solves the Euler equations on a $65 \times 17 \times 7$ grid while the high-fidelity model solves the Navier-Stokes equations on a $193 \times 49 \times 33$ grid.

The optimisation manages to weaken significantly the characteristic lambda shock wave present on the original M6 wing. As a result the drag coefficient is reduced by 26 drag counts, all this achieved while maintaining lift and interior wing volume. The overall aerodynamic coefficients are presented in Table 1 and compared with other Navier-Stokes optimisations found in the literature. Our results

https://doi.org/10.1017/S0001924000001457 Published online by Cambridge University Press

Table 1
Comparison of aerodynamic coefficients obtained for the optimised ONERA M6 wings

	Initial			Optimised			
Origin of data	C_L	C_D	L/D	C_L	C_D	**Improvement in C_D**	L/D
Present work	0·2697	0·01736	15·54	0·2694	0·01478	–14·9%	18·23
Nielsen and Anderson[16]	0·253	0·0168	15·06	0·253	0.0142	–15·5%	17·82
Lee *et al*[50]	0·2622	0·01751	14·97	0·2580	0·01586	–9·4%	16·27
Sung and Kwon[49]	N/A	N/A	N/A	–2·1%	N/A	–12·8%	N/A
Kim and Nakahashi[51]	0·2599	0·01722	15·09	0·2560	0·01611	–6·4%	15·89

compare well with others, proving the validity of the optimisation method. This can now be applied confidently to the optimisation of a BWB aircraft.

5.2 Baseline geometry and optimisation problem

Several aerodynamic optimisations of a BWB are presented in the following sections. They all share the same baseline geometry that serves as a reference for the optimisations. Its planform and key dimensions are shown in Fig. 1. The Navier-Stokes grid around it is shown in Fig. 2. For obvious reasons of symmetry, only a semi-span model is employed. The grid has 161 × 65 × 45 points divided into 16 blocks, defined as the fine Navier-Stokes grid in this study.

The optimisations also have the same flow conditions: Mach number M_∞ = 0·85, unit Reynolds number Re = 6·675 × 10^6 per metre and freestream temperature T_∞ = 218·8K. At the BWB cruise design point, the lift coefficient is required to be 0·41 based on the fixed trapezoidal area of 841·7m^2 that is used to non-dimensionalise all the aerodynamic coefficients. The pitching moment is calculated around the centre of gravity situated 29·3m behind the nose of the aircraft in the plane of symmetry. The reference length used for the pitching moment is the mean aerodynamic chord equal to 12·3m. A positive value of the pitching moment corresponds to a nose down moment.

The different BWB optimisations share the same parameterisation. 16 wing master sections control the BWB shape and are distributed along the span from the centre fuselage to the wing tip before the junction with the winglet. The 15 most inboard master sections are parameterised using 17 design variables each: eight active Bézier parameters for the upper surface, eight for the lower surface and one for the twist increment of that section. The most outboard master section is only allowed to twist with a fixed profile. This is to avoid complication when deforming the wing tip where the winglet is attached. By only allowing twist changes, the winglet follows the changes of the last master section and is thus just rotated in pitch accordingly. In total this makes 256 active design variables (15 × 17 + 1). They are all scaled so that taken in isolation, an increment of 1 in any of the design variable produces a maximum displacement of 2% of the chord of the appropriate master section.

For the optimisations including sweep changes, a design variable controlling the increment in sweep on the BWB wing (from the leading-edge crank to the junction between the wing and winglet) is added. Its scaling coefficient was initially chosen so that an increment of 1 in sweep translates a particular section (situated mid-way, in the spanwise direction, between the leading edge crank and the winglet) by 2% of its chord. However, preliminary testing showed that with such a scaling, the optimisation was not sensitive to sweep, only changing it by a few tenths of a degree at best. To make the optimisation sensitive to sweep, the scaling coefficient related to sweep was arbitrarily set to 40 (a multiplication by 53·7 of the initial coefficient so that an increment of one in sweep translates the middle section by 107·4% of its chord) for the results presented in this paper.

A difference with the M6 wing optimisation mentioned above is the connection between the master sections. Because the centre fuselage is 'fat', linear connections between the master sections do

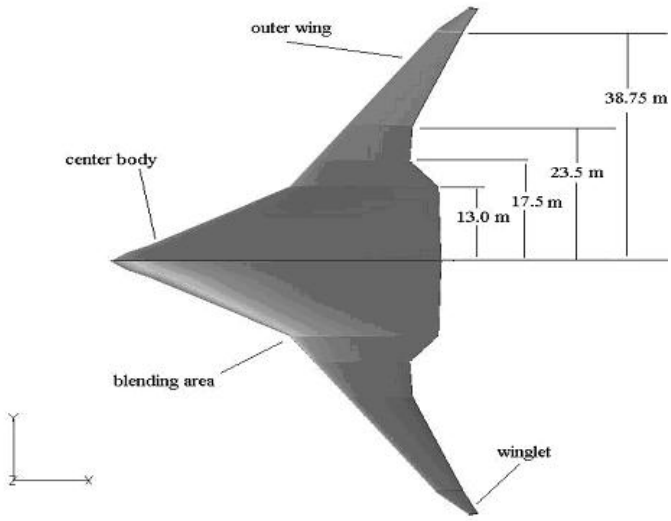


Figure 1. Planform of the baseline BWB geometry.

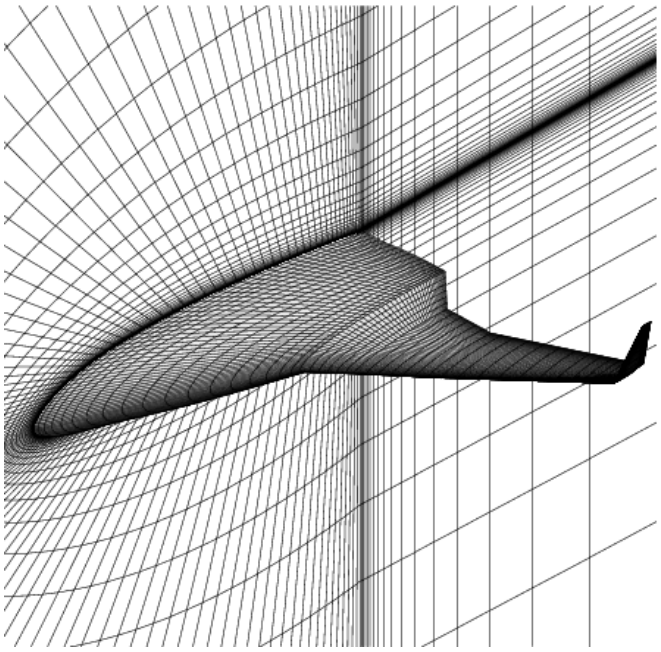


Figure 2. Fine Navier-Stokes grid around the baseline geometry.

https://doi.org/10.1017/S0001924000001457 Published online by Cambridge University Press

not create a smooth shape. Instead piece-wise cubic splines are used to connect the master sections on the fuselage while linear connections are kept on the wing since they are well suited for this kind of geometry.

The optimisation problem is to minimise drag at a constant lift while maintaining the internal volume of the aircraft. This is approximated by the requirements that each master section should maintain its original area. An additional constraint on the pitching moment can also be included depending on the optimisation task. This can be written as:

$$\text{Minimise } C_D$$

$$\text{Subject to: } C_L \geq 0{\cdot}41$$

$$(C_m)^2 \leq (C_{mmax})^2 \quad \text{optional} \qquad \ldots (21)$$

$$V_{0i} \leq V_i \leq 2 \times V_{0i}, \quad i = 1,\ldots,15$$

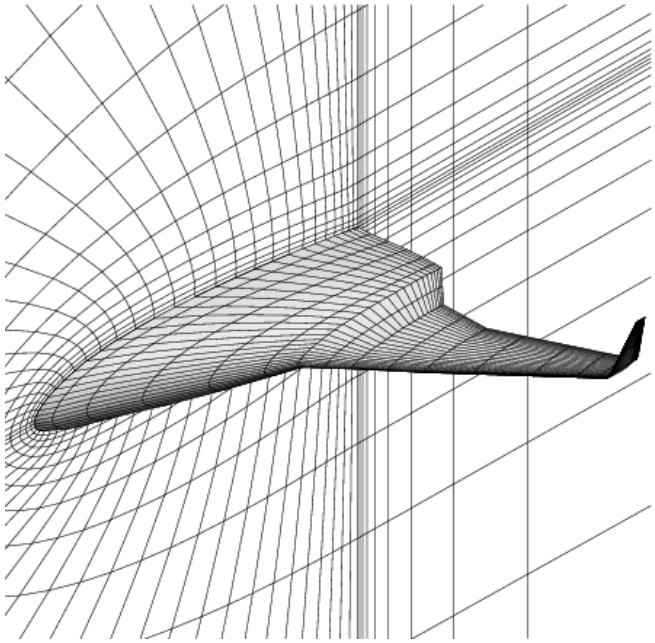
The constraint on the pitching moment is added due to the nature of the BWB as a tailless aircraft. It has thus to be trimmed by deflecting the control surfaces situated along the trailing edge. Some calculations done at NLR for the MOB project[52] found that the trim drag i.e. the drag generated by the necessary deflection of the control surfaces to trim the aircraft, was very penalising. Hence it would be better if the BWB shape was trimmed naturally or required very small control surface deflections during the cruise condition. This is why the constraint on the pitching moment is included that aims at forcing the pitching moment to stay close to zero to get a nearly trimmed aircraft. However this constraint is limiting. We will see that it reduces the potential improvements in L/D. In addition a consistent longitudinal stability analysis should include the effect of thrust, which has not been taken into account in this study.

The flow and adjoint solutions employed in the optimisations of the BWB are required to converge to five orders. More specifically, the flow solutions stop after 5,000 implicit iterations or when reaching five orders of convergence, while the adjoint solutions are stopped after 3,000 iterations or when reaching five orders of convergence. Although convergence occurs for most of the flow and adjoint solutions, there were cases when the solutions could not reach five orders of reduction before the maximum number of iterations was reached. While allowing some partially converged solutions in the process is not ideal, it is necessary for the robustness and practicality of the optimisation procedure. All the computations restart from previous solutions to save some computing time and the optimisations start from converged flow and adjoint solutions calculated on the baseline geometry with the grids and physical models employed in these optimisations.

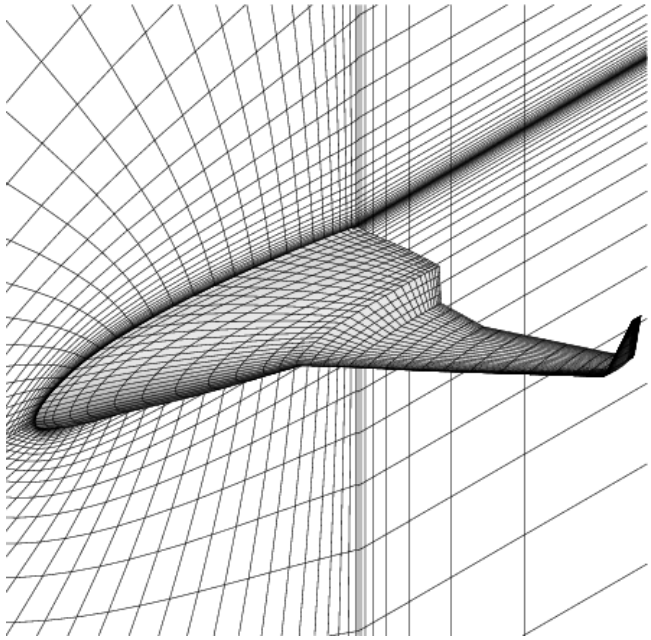
5.3 Optimisations of the BWB shape through master section profiles

Two Euler optimisations of the BWB are presented in this section, one including the constraint on pitching moment with $C_{mmax} = 0{\cdot}001$, the other without it. They only modify the shape and twist of the master sections, the wing planform remains fixed. They use the variable-fidelity method even though the low- and high-fidelity models solve the same Euler equations. The low-fidelity model uses a coarse Euler grid with 81 × 17 × 22 points divided into 16 blocks while the high-fidelity model employs a finer Euler grid with 81 × 33 × 39 points also divided into 16 blocks. These two grids are shown in Fig. 3.

The optimisation histories are shown in Fig. 4. The merit function shown is used in the variable fidelity method to assess the 'quality' of the design points obtained after each low-fidelity optimisation: it is the sum of the objective function and of penalty terms related to the constraints, all of them calculated on the high-fidelity model. In Fig. 4(a) it is non-dimensionalised by its initial value. This is done in order to plot on the same graph the merit functions of the two optimisations which have different magnitudes. The optimisation histories show that the two optimisations are successful for drag reduction. The merit function Φ_{hi} is reduced, which is reflected by a decrease in drag coefficient while the lift constraint is satisfied. The pitching moment is greatly reduced and much closer to zero than for the initial geometry when the pitching moment constraint is included. However this constraint is not strictly satisfied. This is



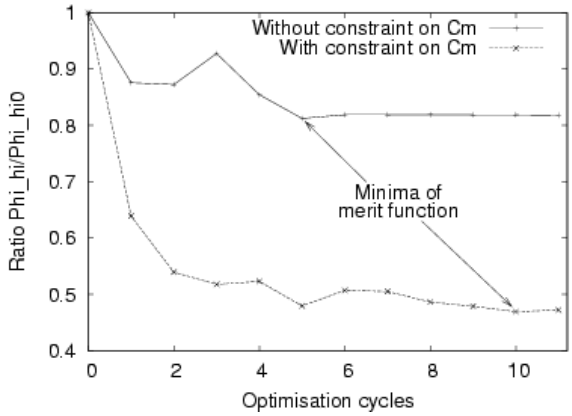
(a) Low-fidelity Euler grid



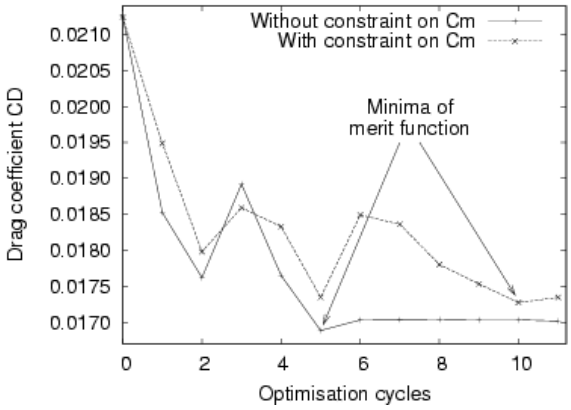
(b) High-fidelity Euler grid

Figure 3. The two grid levels used for the Euler optimisations of the BWB.

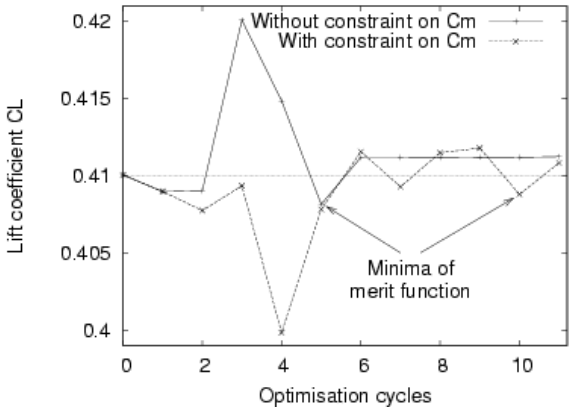
https://doi.org/10.1017/S0001924000001457 Published online by Cambridge University Press



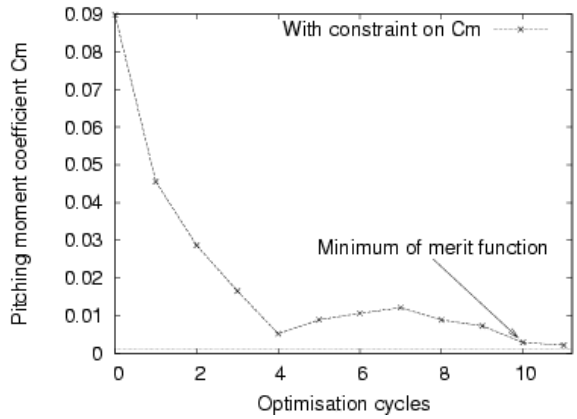
(a) Ratio of merit function Φ_{hi}/Φ_{hi0}



(b) Drag coefficient C_D



(c) Lift coefficient C_L



(d) Pitching moment coefficient C_m for the optimisation with constraint

Figure 4. Evolution of different parameters during the variable-fidelity optimisations of the BWB.

because the variable fidelity method is not a feasible optimisation method and in this case it cannot find a feasible point.

The aerodynamic coefficients of the optimised geometries compared to the initial one are given in Table 2. These are calculated at the exact target C_L of 0·41 to enable a fair comparison between the geometries. Table 2 confirms the improvement in performance gained by the two optimisations. As expected and seen in Fig. 4 the constraint on pitching moment slightly limits the improvement. However, the loss in L/D is probably compensated by the very low pitching moment obtained since we can see that the other optimisation is dragging the design away from a trimmed aircraft for only a small gain in performance.

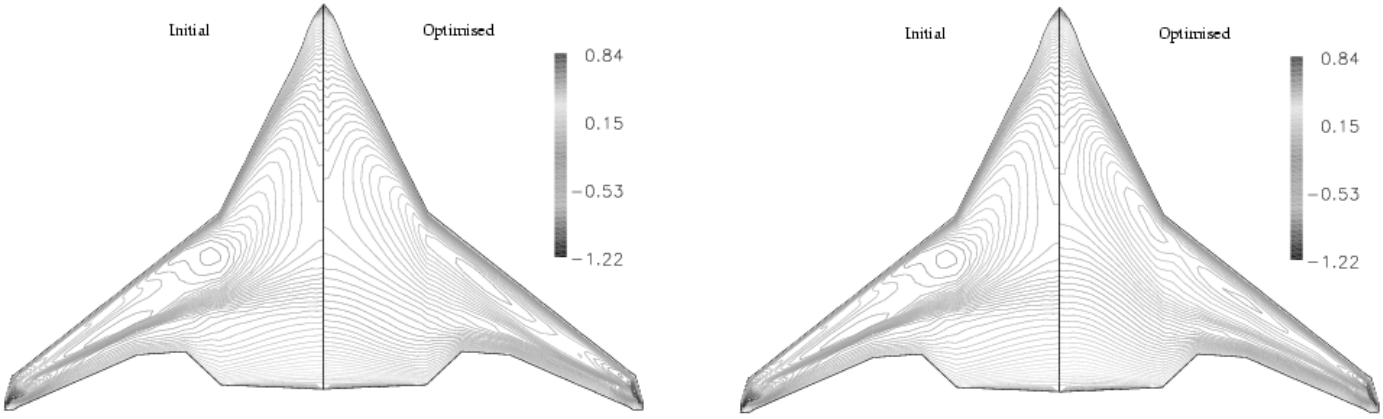
Figure 5 compares the pressure distribution of the initial geometry with that of the optimised BWBs. This is obtained in the inviscid mode on the fine Euler grid. On the initial geometry a very strong shock wave spans the whole wing up to the fuselage. The optimisations clearly manage to weaken this shock wave that has now disappeared on the fuselage. It seems that they have however reinforced it at the wing tip where the interaction with the winglet shock, still present and very strong, is more pronounced. This is believed to be the result of the fixed profile at the junction and the fixed winglet shape.

This overall picture is completed by the chordwise pressure distributions given at six spanwise locations shown in Fig. 6. Some interesting features are worth mentioning. As noticed above, the shock wave has been eliminated on some part of the wing as can clearly be seen at the station $\eta = 0{\cdot}40$. As we move further outboard on the wing, a shock wave starts to form and is even stronger than on the initial geometry (station at $\eta = 0{\cdot}93$). The last station at 98% of the span i.e. very close to the junction between the wing and winglet shows the disturbed flow field in this region with strange pressure distributions. Overall the aircraft with constraint on pitching moment carries less lift than the other optimised BWB on the rear part of the

Table 2
Inviscid aerodynamic coefficients of the Euler optimised BWBs

Geometry	C_L	C_D	L/D	C_m
Initial	0·4100	0·02109	19·44	0·08957
Optimised, without constraint on C_m	0·4100	0·01697	24·16	0·14008
Optimised, with constraint on C_m	0·4101	0·01733	23·66	0·00338

https://doi.org/10.1017/S0001924000001457 Published online by Cambridge University Press



(a) Without constraint on C_m

(b) With constraint on C_m

Figure 5. Comparison of the contours of pressure coefficient on the upper surface of the initial and optimised BWBs. Euler calculations.

sections (after 60% chord say) for all the stations. On the fuselage, it carries more negative lift at the rear of the sections (root section and station at $\eta = 0{\cdot}17$) than the baseline geometry. Effectively it produces more negative reflexed camber in the centre section as explained below. Furthermore the shock wave on the constrained optimised BWB is situated further forward on the wing than for the unconstrained BWB. All of these give an explanation as to how the low pitching moment is achieved: removing some lift on the rear part of the sections reduces the nose down pitching moment around the centre of gravity. Obviously carrying negative lift on some part of the fuselage is detrimental from a pure aerodynamic design point of view but this is how the optimisation manages to trim the aircraft.

The shape deformations shown in Fig. 7 also explain how this is achieved. Note first that the sections are shown in their true coordinates that are non-dimensionalised by the chord of the root section. The sections are thus seen in their twisted position. However the scale on the vertical axis is very different from the one on the horizontal axis, which gives the impression that the outer wing sections are twisted at 45° while it is only 6 or 7° in reality. On the fuselage, the twist is decreased and the reverse camber on the rear of the profile is increased. It is interesting to note that in Ref. 25 Mialon *et al* avoided using profiles with negative aft camber on the fuselage of their first configuration, probably in order not to create negative lift as mentioned above, but as a result did not manage to trim their BWB. Hence it seems that reverse camber on the fuselage of the BWB plays a key role in the aircraft trim.

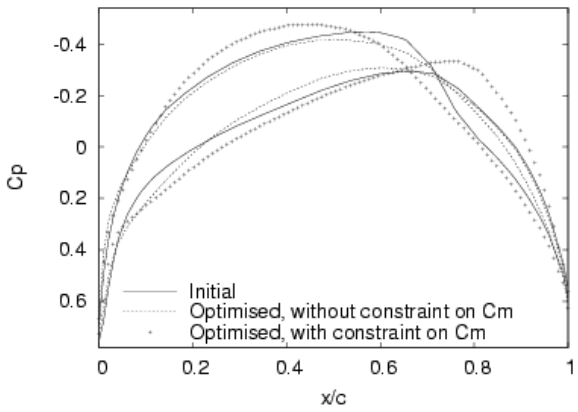
On the rest of the wing, both optimisations modify the shape in the same way: on the inner part of the wing ($0{\cdot}40 \leq \eta \leq 0{\cdot}71$), the rear part of the sections is thickened by transferring some volume from the lower surface leading edge region to the rear of the aerofoil on the upper surface. This moves the point of maximum thickness backwards and reduces the leading edge radius. Note that this behaviour is more pronounced on the pitch constrained geometry with the creation of a drooped nose at $\eta = 0{\cdot}71$. As can be seen in the corresponding pressure distribution of Fig. 6, its effect is to increase the lift carried by the leading edge, while pushing the maximum thickness backwards reduces the loading on the rear of the aerofoil. This explains geometrically how the low pitching moment is obtained by pushing the lift forwards as mentioned earlier. At the wing tip the opposite occurs with thick leading edges and very thin and pointed rear parts. This is believed to be a result of the interaction between the outer wing and the winglet due to local strong compressibility effects.

There is little change in the twist angles, which can be seen with the spanwise twist distributions of Fig. 8. The main difference between the two optimisations occurs on the fuselage where the constraint on pitching moment leads to a nose-up increment in twist while the other optimisation increases slightly the nose-down twist as can be seen from Fig. 7. On the rest of the wing, the optimisations increase the nose-down twist as could also be seen from the wing profiles. These twist changes are however very small compared to the twist redesign exercise of Ref. 31 but the optimiser has the additional freedom of modifying the aerofoil shapes to get where it wants to go so the twist angles might not play such an important role. In other words, the aerodynamic twist seems to be more effective than the geometrical twist in this case.

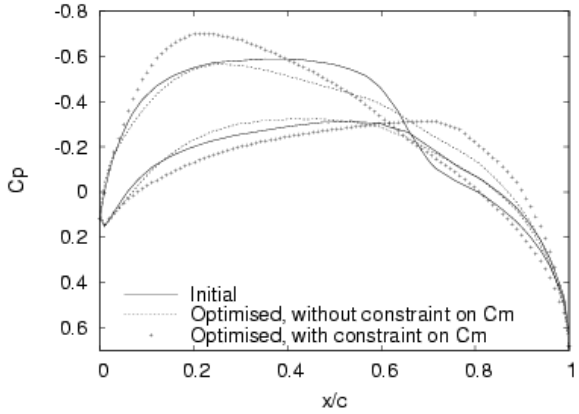
Figure 9 shows the spanwise loading distribution of the baseline and optimised geometries. These are compared to theoretical elliptic and triangular distributions to make a parallel with our earlier work in Ref. 31. The optimisations do not alter significantly the lift distribution when compared to the big difference between the elliptic and triangular distributions. All three distributions are surprisingly very close to the elliptic loading, the curve corresponding to the unconstrained optimisation being almost on top of the elliptic curve. Thus it seems that the optimisation aims at reproducing an elliptic loading. Since the initial geometry is not far from this, only small adjustments are made. These are similar for the two optimisations. They consist in a transfer of lift from the middle of the fuselage to the outer part of the fuselage and a relief of the wing tip loading that is evenly redistributed on the wing. The change of lift on the fuselage, at least for the pitch constrained aircraft, is due to the reverse cambered aerofoils on the centre part, while the reduction of wing tip loading 'tidies up' the flowfield in this region of strong interaction with the winglet.

The improvements in L/D are substantial as seen before, at least in the Euler mode. What has been presented so far for these two optimisations shows that they are successful. Starting from a given Euler grid and flow solution, the optimisations have managed to find much better design points while satisfying the constraints or at least improving on them. But is it still the case when transferred to the fine Navier-Stokes grid? This is now the point of view of the aerodynamicist who wants to know if the optimisation has managed to improve the starting geometry. The answer is given in Table 3 where the design changes obtained by the Euler optimisations are applied to the fine Navier-Stokes grid of Fig. 2 that is then solved by the RANS solver to assess the aircraft performance. Table 3 shows that the improvements are also substantial in the Navier-Stokes mode and that the trends observed in the Euler mode are carried over in the Navier-Stokes mode. The first point is that the improvements on the aircraft resulting from the optimisation without constraint on C_m are slightly higher than on the other optimised BWB. An improvement

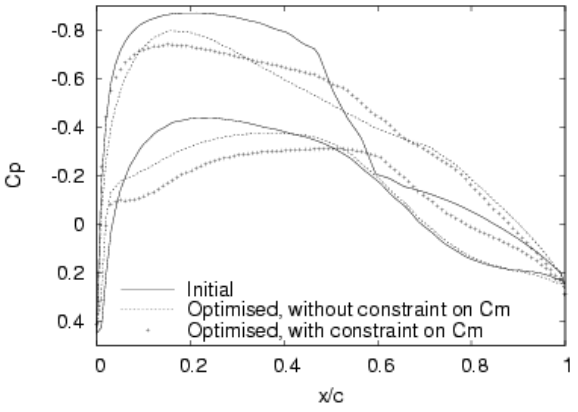
https://doi.org/10.1017/S0001924000001457 Published online by Cambridge University Press



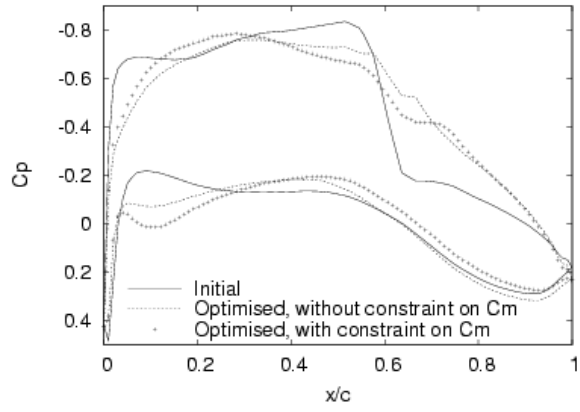
(a) Root section



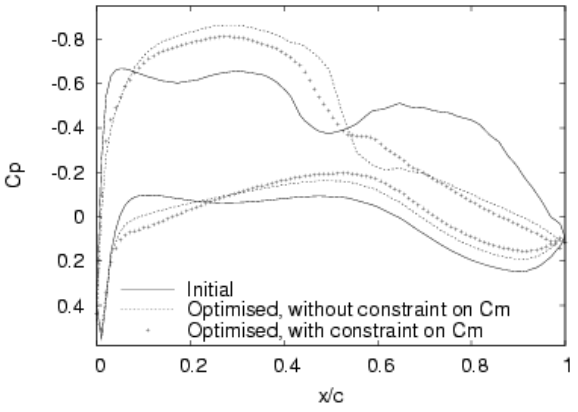
(b) Fourth master section at $\eta = 0{\cdot}17$



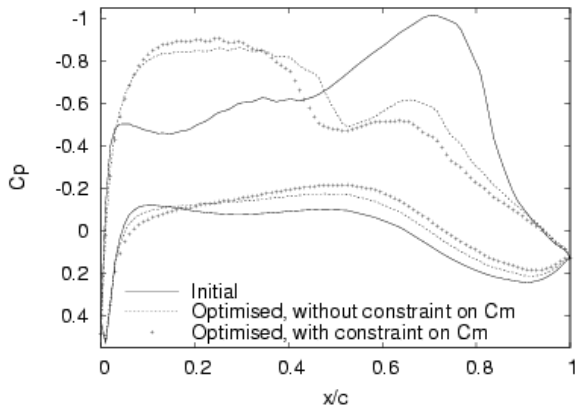
(c) Eighth master section at $\eta = 0{\cdot}40$



(d) 12th master section at $\eta = 0{\cdot}71$



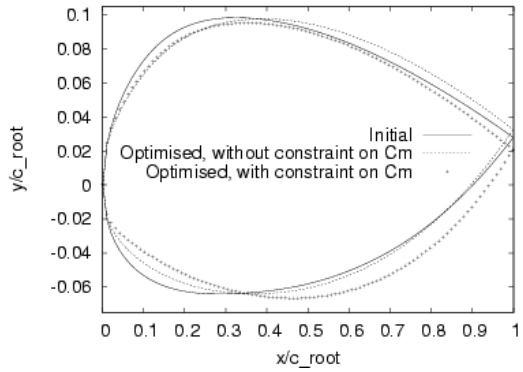
(e) 14th master section at $\eta = 0{\cdot}93$



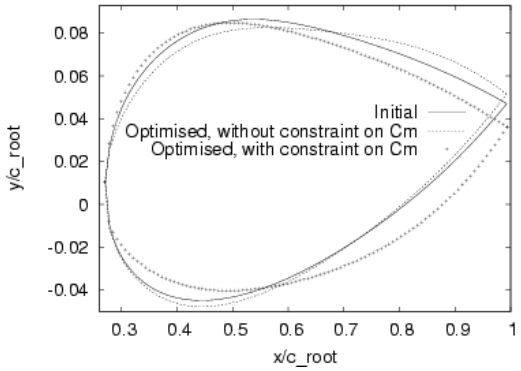
(f) 15th master section at $\eta = 0{\cdot}98$

Figure 6. Chordwise C_p distributions on some master sections for the optimised BWBs. Euler calculations.

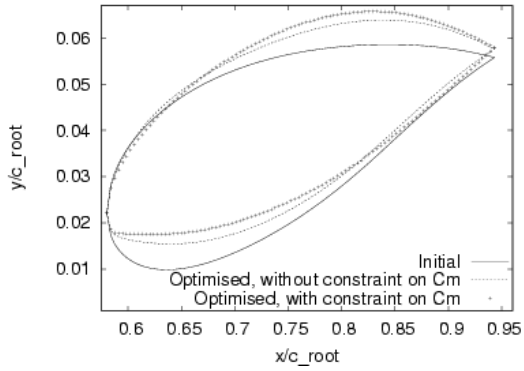
https://doi.org/10.1017/S0001924000001457 Published online by Cambridge University Press



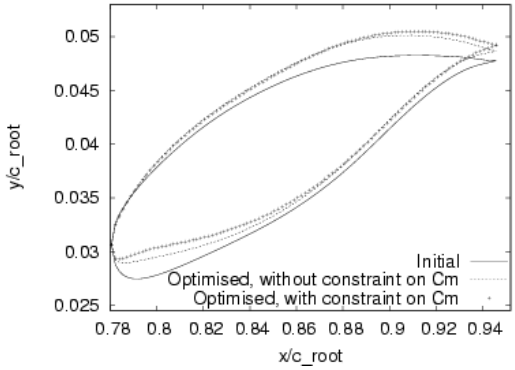
(a) Root section



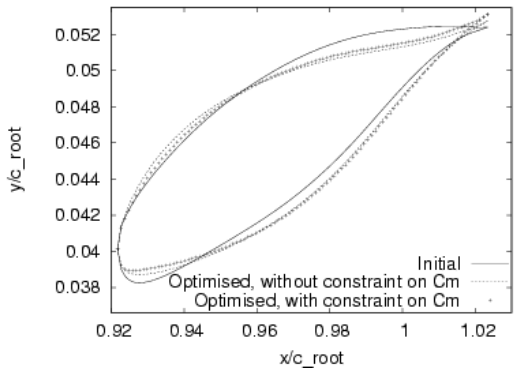
(b) Fourth master section at $\eta = 0{\cdot}17$



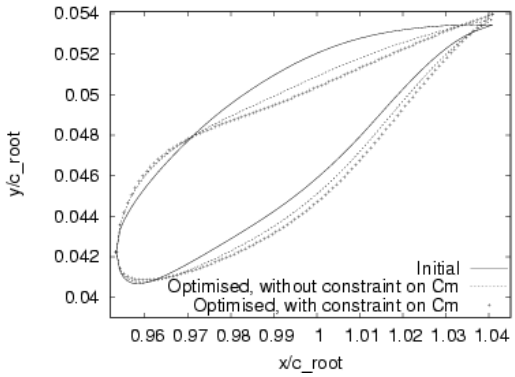
(c) Eighth master section at $\eta = 0{\cdot}40$



(d) 12th master section at $\eta = 0{\cdot}71$



(e) 14th master section at $\eta = 0{\cdot}93$



(f) 15th master section at $\eta = 0{\cdot}98$

Figure 7. Shape modification of some master sections for the optimised BWBs.

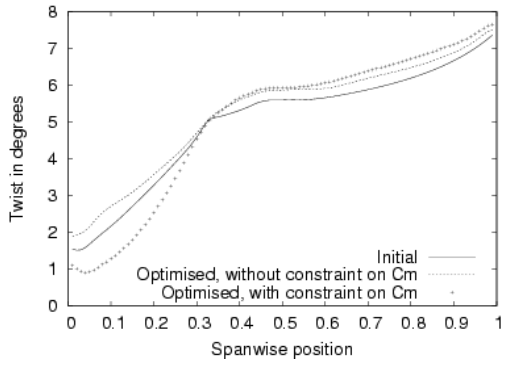


Figure 8. Spanwise twist distribution in degrees for the optimised BWBs.

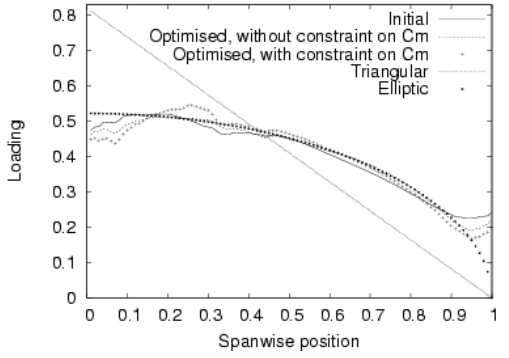
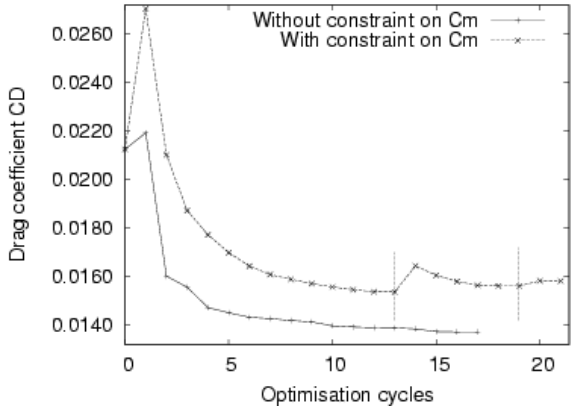


Figure 9. Spanwise loading ($C_{L\ local} \times (c/\overline{c})$) for the optimised BWBs compared to triangular and elliptic loadings. Euler calculations.

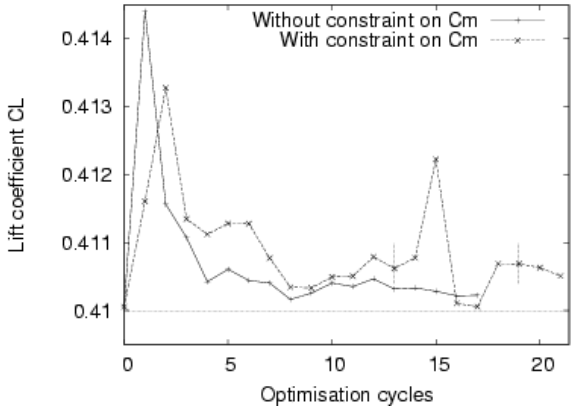
https://doi.org/10.1017/S0001924000001457 Published online by Cambridge University Press

Table 3
Navier-Stokes check on the fine Navier-Stokes grid of the Euler optimised BWBs

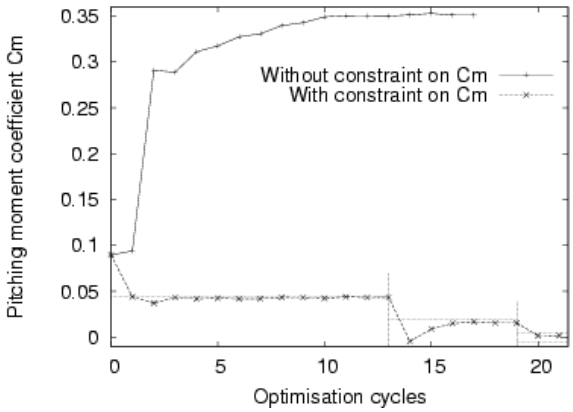
Geometry	C_L	$C_{D\ total}$	$C_{D\ press}$	$C_{D\ fric}$	$C_{D\ wave}$	L/D	C_m
Initial reference	0·4101	0·02855	0·01885	0·00969	0·00101	14·37	0·07360
Without constraint on C_m	0·4101	0·02576	0·01581	0·00995	0·00042	15·92	0·11533
With constraint on C_m	0·4100	0·02595	0·01592	0·01003	0·00023	15·80	–0·00401



(a) Drag coefficient C_D



(b) Lift coefficient C_L



(c) Pitching moment coefficient C_m

Figure 10. Evolution of different parameters during the direct optimisations of the BWB with sweep angle change.

of up to 28 drag counts is achieved i.e. a reduction of 10% of the total drag. In both cases, the improvements are obtained by a reduction of the pressure drag, part of it coming from a lower wave drag. Since the wetted area should not be changed very much by the optimisations, there is little change in the skin friction drag. It is also reassuring to see that the behaviour observed in the Euler mode for the pitching moment is well reflected by the Navier-Stokes checks for the two optimisations. We have a substantial increase in pitching moment for the optimisation without constraint and almost a longitudinally trimmed aircraft resulting from the other optimisation. This shows that the Euler optimisation is a very efficient tool to perform optimisation since it is relatively fast and still provides substantial improvements at a higher level of fidelity which is more relevant to the designer.

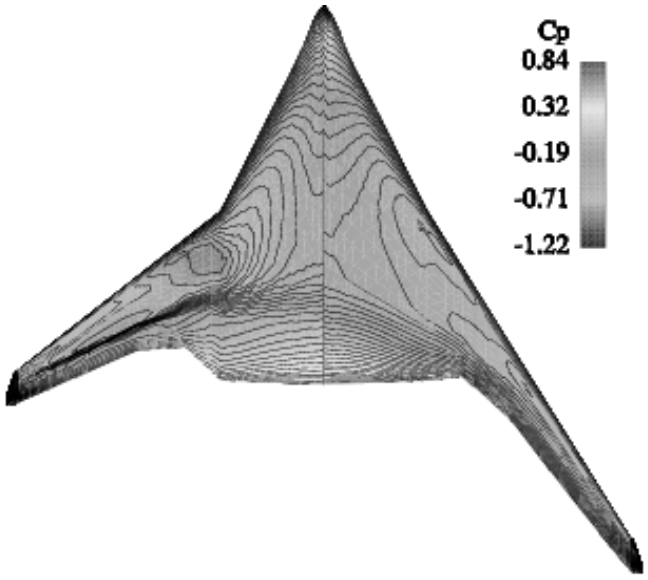
5.4 Optimisations of the BWB shape and outer wing sweep angle

Two further Euler optimisations of the BWB are presented in this section. As in the previous section, one is with constraint on pitching moment, the other without. The difference from the two optimisations already discussed is the addition of a design variable controlling the increment in leading edge sweep angle on the outer wing of the BWB. Both optimisations are run in the Euler mode on the high-fidelity grid shown in Fig. 3(b).

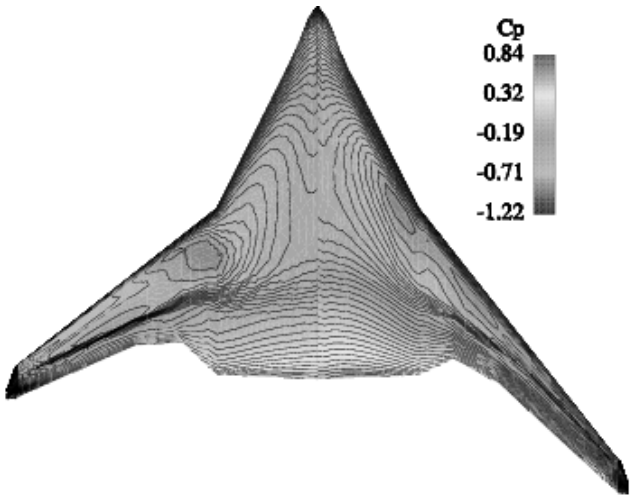
For the optimisation with constraint on C_m, a direct optimisation with a low value of $C_{m\ max}$ did not work because the optimiser FFSQP could not find a feasible point starting from the baseline geometry. To overcome this, a series of three optimisations was performed where the value of $C_{m\ max}$ was reduced progressively, each optimisation starting from the best design point found by the previous one. The first optimisation used $C_{m\ max} = 0{\cdot}045$ (approximately half of the initial pitching moment coefficient), the second $C_{m\ max} = 0{\cdot}020$ (another reduction by half) and the final one $C_{m\ max} = 0{\cdot}005$ to get a nearly trimmed BWB.

The history of both optimisations is detailed in Fig. 10. On the three graphs, the vertical bars for the optimisation with constraint on pitching moment mark the change in the value of $C_{m\ max}$. As can be seen in Fig. 10(a), this change has a slightly negative effect on the evolution of the drag coefficient as could be expected from the results of the previous optimisations with fixed planform. Both optimisations work well. A substantial reduction in drag is obtained while the constraints on lift and pitching moment are satisfied. The latter point is expected since FFSQP is a feasible algorithm as can be seen in the histories where the constraints are satisfied at each design iteration.

https://doi.org/10.1017/S0001924000001457 Published online by Cambridge University Press



(a) Without constraint on C_m



(b) With constraint on C_m

Figure 11. Comparison of the contours of pressure coefficient on the upper surface of the initial (left) and optimised (right) BWBs with sweep angle change. Euler calculations.

The final aerodynamic coefficients are given in Table 4. The addition of a degree of freedom through the sweep angle brings some significant improvement compared to the results of Table 2. A lift to drag ratio of almost 30 is reached i.e. more than a 50% improvement from the baseline geometry. However as happened for the optimisations of the previous section, this is achieved at the expense of the increased pitching moment, which reaches a high value of nose down pitching. As seen from Fig. 10(a), the optimisation with constraint on C_m does not reduce drag as much as the other one, but it manages to trim the aircraft and still improves on the optima of Table 2.

The planform changes are shown in Fig. 11. The baseline geometry has a leading edge sweep angle of 38·3°. The optimisation without constraint on C_m has increased it by 20·0° giving a sweep angle of 58·3°, very close to the fuselage sweep angle of 63·6°. The optimisation with constraint on pitching moment results in an outer wing sweep angle of 51·7° (an increase of 13·4°).

Figure 11 also shows the pressure distribution on the upper surface of the geometries. By sweeping the wing so much, the optimisation without constraint has managed to remove the shock wave from the entire wing. On the other optimised geometry a shock wave is still present but much weaker than that on the baseline geometry. The details of the pressure distribution are plotted in Fig. 12 at the same spanwise stations as before. Some of the features explained in the previous section are still present here and are further amplified. First, the nearly trimmed aircraft carries a lot of negative lift on the rear part of the fuselage to achieve this balance in pitch. As a result the root section appears to contribute very little to lift, opposite to what we desire for a BWB design. Second, on the rest of the wing for this aircraft, most of the lift is carried on the front part of the sections with a strong suction peak terminated by a weak shock wave. On the other optimised geometry, evidence is given here that the shock wave has been completely eliminated. This is remarkable when looking at the section at $\eta = 0{\cdot}71$ where there is a very strong shock wave on the initial geometry.

The wing sections plotted in Fig. 13 have some commonality with those of Fig. 7. The reverse camber is obvious on the fuselage profiles of the trimmed aircraft (root and station $\eta = 0{\cdot}17$), even more pronounced than before in order to counteract the strong nose down pitching moment generated by the highly swept wing. On the rest of the wing, both aircraft have similar profiles. On the middle part of the wing, some thickness is transferred from the pressure side of the leading edge to the middle part of the upper surface. At $\eta = 0{\cdot}71$, a drooped leading edge is created again on the pitch constrained geometry. Its effect on the pressure on the lower surface is also visible in Fig. 12. Towards the wing tip, profiles with very thin trailing edge are created again.

The twist distribution of Fig. 14 shows that some significant retwist occurred on the fuselage of the trimmed aircraft. The twist changes are bigger than for the geometries of the previous section (Fig. 8) but the trend is the same: a nose-up twist on the fuselage to trim the aircraft. On the outer wing, the initial twist distribution is kept almost unchanged on both aircraft.

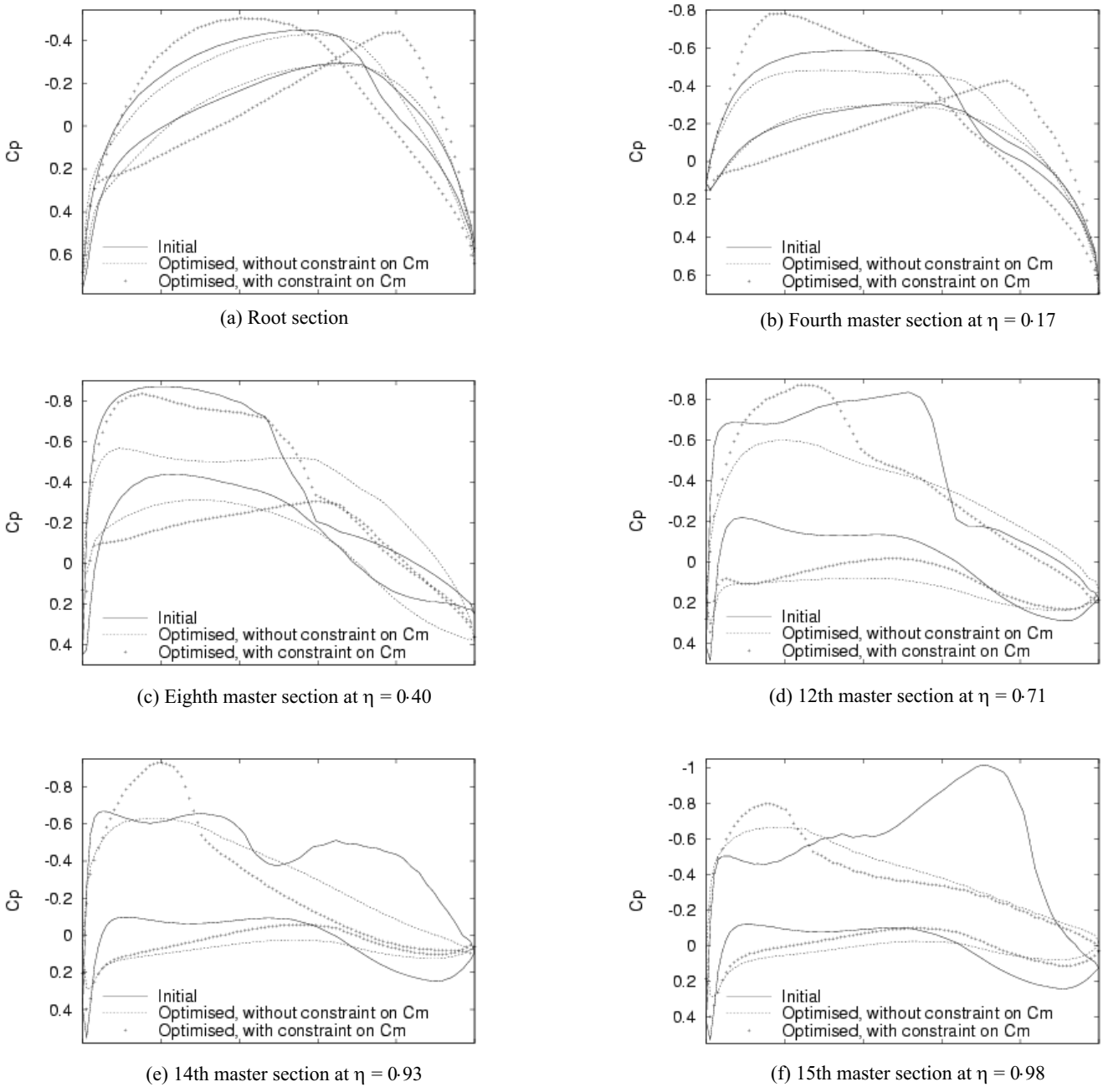
Despite huge changes in the BWB planform, the spanwise loading distributions shown in Fig. 15 are very similar to those obtained with the fixed baseline planform. All three are close to the elliptic distribution, the closest being once more the geometry optimised without constraint on C_m. The same transfers of lift from the centre fuselage to the outer fuselage and from the wing tip to the rest of the wing can be seen.

As before, a Navier-Stokes calculation on a fine grid around the Euler optimised geometries was carried out to check if the changes were transferred to this higher level of modelling. The corresponding aerodynamic coefficients are given in Table 5. We can see that the trend in the inviscid mode has been carried forward in the Navier-Stokes mode. The optimisation without constraint on Cm achieves a very good improvement in L/D but at the cost of a very high pitching

Table 4
Inviscid aerodynamic coefficients of the Euler optimised BWBs with sweep angle change

Geometry	C_L	C_D	L/D	C_m
Initial	0·4100	0·02109	19·44	0·08957
Optimised, without constraint on C_m	0·4100	0·01371	29·90	0·35093
Optimised, with constraint on C_m	0·4100	0·01580	25·96	0·00169

https://doi.org/10.1017/S0001924000001457 Published online by Cambridge University Press



(a) Root section

(b) Fourth master section at $\eta = 0{\cdot}17$

(c) Eighth master section at $\eta = 0{\cdot}40$

(d) 12th master section at $\eta = 0{\cdot}71$

(e) 14th master section at $\eta = 0{\cdot}93$

(f) 15th master section at $\eta = 0{\cdot}98$

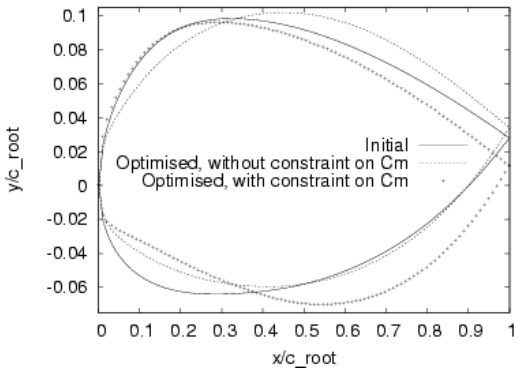
Figure 12. Chordwise C_p distributions on some master sections for the optimised BWBs with sweep angle change. Euler calculations.

moment once more, whereas the geometry obtained by the other optimisation is also nearly trimmed in the Navier-Stokes mode with a gain in performance. The drag breakdown shows a bigger increase in friction drag than previously. This is considered to be caused by the elongation of the wing due to the increased sweep angle. Although the planform area is unchanged, the wetted area slightly increases (to view this, consider the external surface of a cube being deformed by shear in one direction).

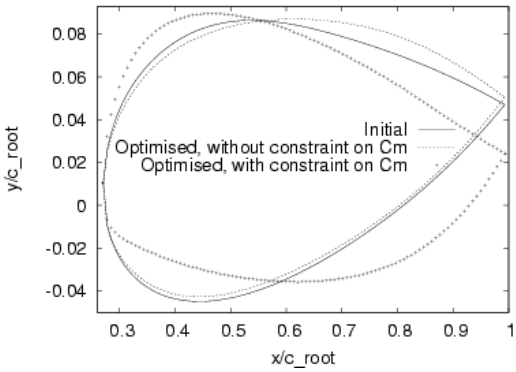
6.0 SUMMARY AND CONCLUSION

Aerodynamic shape optimisations of a blended wing body have been described in this article. These optimisations use a discrete adjoint solver to compute efficiently the sensitivity derivatives needed by the gradient-based optimisation algorithms. These are either a direct sequential quadratic programming method or a variable fidelity method. The optimisations modify a series of master sections (section profile and twist) defining the BWB geometry. The leading

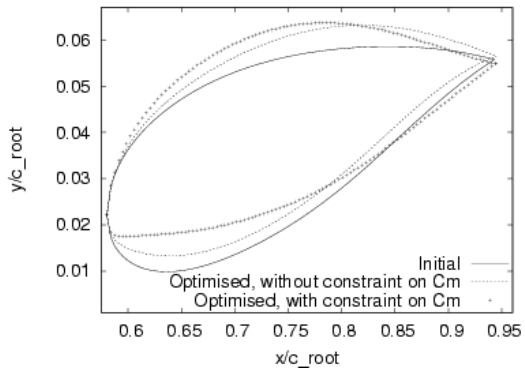
https://doi.org/10.1017/S0001924000001457 Published online by Cambridge University Press



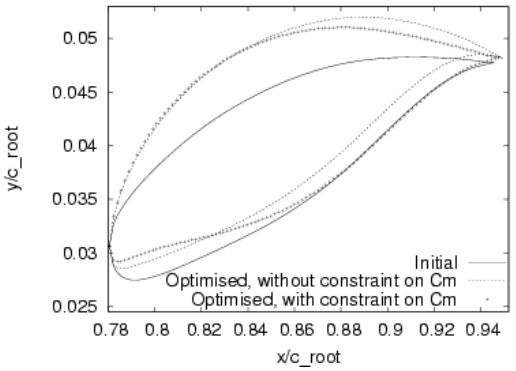
(a) Root section



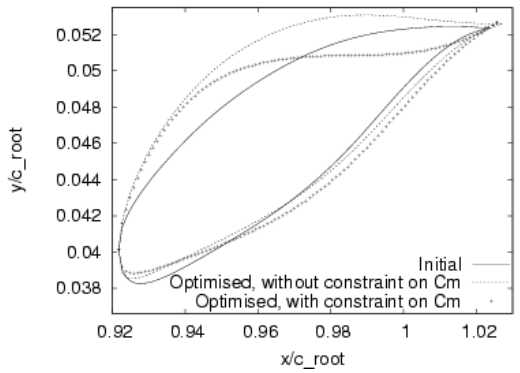
(b) Fourth master section at $\eta = 0{\cdot}17$



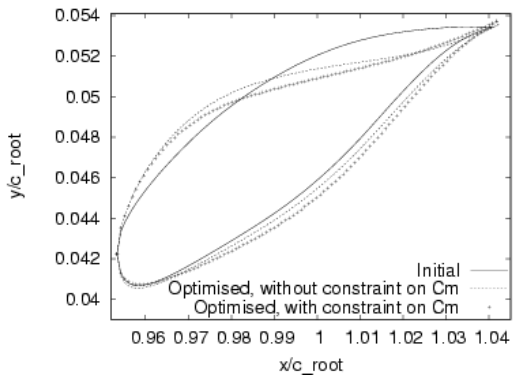
(c) Eighth master section at $\eta = 0{\cdot}40$



(d) 12th master section at $\eta = 0{\cdot}71$



(e) 14th master section at $\eta = 0{\cdot}93$



(f) 15th master section at $\eta = 0{\cdot}98$

Figure 13. Shape modification of some master sections for the optimised BWBs with sweep angle change.

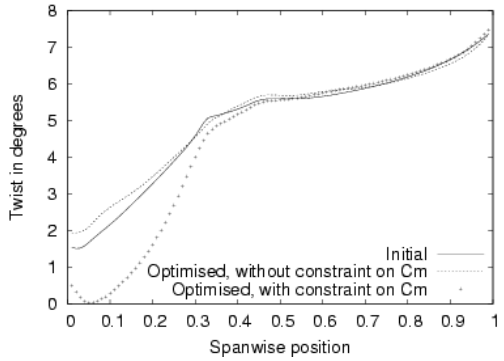


Figure 14. Spanwise twist distribution in degrees for the optimised BWBs with sweep angle change.

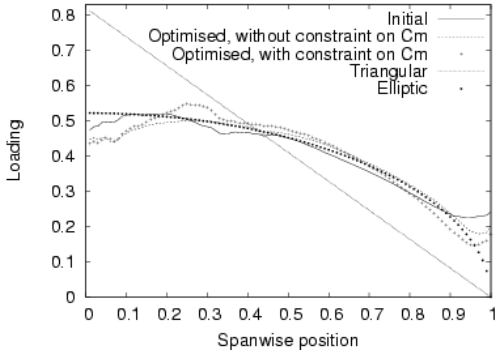


Figure 15. Spanwise loading ($C_{L\ local} \times (c/\bar{c})$) for the optimised BWBs with sweep angle change compared to triangular and elliptic loadings. Euler calculations.

https://doi.org/10.1017/S0001924000001457 Published online by Cambridge University Press

Table 5
Navier-Stokes check on the fine Navier-Stokes grid of the Euler optimised BWBs with sweep angle change

Geometry	C_L	$C_{D\ total}$	$C_{D\ press}$	$C_{D\ fric}$	L/D	C_m
Initial reference	0·4101	0·02855	0·01885	0·00969	14·37	0·07360
Without constraint on C_m	0·4100	0·02401	0·01356	0·01044	17·08	0·31559
With constraint on C_m	0·4100	0·02580	0·01518	0·01062	15·89	0·00703

edge sweep angle on the outer wing is allowed to change, which alters the planform of the aircraft. All the optimisations presented are successful in the sense that they manage to reduce substantially the drag coefficient while satisfying the constraint on lift coefficient and the trim constraint when the latter is included as a constraint.

These optimisations are performed in the Euler mode but it has been shown in this article that the improvements are carried over when the optimised geometries are computed in the Navier-Stokes mode on an appropriate grid. The decrease in drag is also substantial. When the aircraft is naturally trimmed in the Euler mode, it is also in the Navier-Stokes mode. This is the main conclusion of this article that Euler optimisations are a very useful and cost-effective optimisation tool since the improvements obtained are transferred to a higher level of modelling. This is because the flow physics for drag reduction and trim for the present cases is primarily inviscid.

These BWB optimisations are only single discipline optimisations. A multi-disciplinary approach involving at least flight dynamics and structures would be more relevant for this tailless aircraft where wing and fuselage are all integrated into one part. This is particularly true for the optimisations involving sweep angle changes where aerodynamics seems to favour a more swept back wing. From a structural point of view, increasing the sweep angle means increasing the structures strength and hence weight to overcome the increase in bending moment so it is not necessarily a good design choice. It is intended to carry on this work on BWB optimisation by incorporating a constraint on bending moment, obtained from a simplified structural model, to account for this trade-off and obtain more realistic geometries.

ACKNOWLEDGEMENTS

Part of this work was funded by a Scholarship from Cranfield College of Aeronautics, UK and the EU under the Growth Programme Contract No G4RD-CT1999-0172 for the MOB project. The optimisations involving sweep angle changes were performed on the HPCx machine. The HPCx computer time was provided through the UK Applied Aerodynamics Consortium (UKAAC) under EPSRC grant GR/S91130/01. The authors acknowledge AEMDesign for kindly providing the optimiser FFSQP used in the present work.

REFERENCES

1. PORTSDAM, M.A., PAGE, M.A. and LIEBECK, R.H. Blended wing body analysis and design, June 1997, AIAA Paper 1997-2317.
2. LIEBECK, R.H., PAGE, M.A. and RAWDON, B.K. Blended-wing-body subsonic commercial transport, January 1998, AIAA Paper 1998-438.
3. LIEBECK, R. Design of the blended-wing-body subsonic transport, *J Aircr*, January-February 2004, **41**, pp 10–25.
4. SMITH, H. College of aeronautics blended wing body development programme, 2000, 22nd International Congress of Aeronautical Sciences, ICAS-2000-1.1.4, Harrogate, UK, 27 August-1 September 2000.
5. PAMBAGJO, T., NAKAHASHI, K., OBAYASHI, S. and MATSUSHIMA, K. Aerodynamic design of a medium size blended-wing-body airplane, January 2001, AIAA Paper 2001-0129.
6. BOLSUNOVSKY, A., BUZOVERYA, N., GUREVICH, B., DENISOV, V., DUNAEVSKY, A., SHKADOV, L., SONIN, O., UDZHUHU, A. and ZHURIHIN, J. Flying wing — problems and decisions, *Aircraft Design*, 2001, **4**, pp 193–219.
7. MORRIS, A. MOB a European distributed multi-disciplinary design and optimisation project, September 2002, AIAA Paper 2002-5444.
8. MIALON, B. and HEPPERLE, M. Flying wing aerodynamics studies at ONERA and DLR, 2005, CEAS/KATnet Conference on Key Aerodynamic Technologies, Bremen, Germany, 20-22 June 2005.
9. JIMÉNEZ-VARONA, J. Design of blended-wing-body configurations using a constrained numerical optimisation method, 2005, CEAS/KATnet Conference on Key Aerodynamic Technologies, Bremen, Germany, 20-22 June 2005.
10. JAMESON, A. Aerodynamic design via control theory, *J Scientific Computing*, 1988, **3**, (3), pp 233–260.
11. REUTHER, J., JAMESON, A., FARMER, J., MARTINELLI, L. and SAUNDERS, D. Aerodynamic shape optimization of complex aircraft configurations via an adjoint formulation, January 1996, AIAA Paper 96-0094.
12. REUTHER, J., JAMESON, A., ALONSO, J.J., RIMLINGER, M.J. and SAUNDERS, D. Constrained multipoint aerodynamic shape optimization using an adjoint formulation and parallel computers, *AIAA J*, January-February 1999, **36**, (1), pp 51–74.
13. JAMESON, A., PIERCE, N.A. and MARTINELLI, L. Optimum aerodynamic design using the Navier-Stokes equations, *Theoretical and Computational Fluid Dynamics*, January 1998, **10**, (1-4), pp 213–237.
14. GILES, M.B., DUTA, M.C. and MULLER, J.-D. Adjoint code developments using the exact discrete approach, June 2001, AIAA Paper 2001-2596.
15. KIM, C.S., KIM, C. and RHO, O.-H. Aerodynamic sensitivity analysis for turbulent flows on chimera overlaid grids, *AIAA J*, May 2001, **39**, (5), pp 838–845.
16. NIELSEN, E.J. and ANDERSON, W.K. Recent improvements in aerodynamic design optimization on unstructured meshes, *AIAA J*, June 2002, **40**, (6), pp 1155–1163.
17. CORMERY, M. Adjoint operator approach to aerodynamic shape optimisation for 3D transonic flows, 1998, *Proceedings of the 4th European Computational Fluid Dynamics Conference ECCOMAS 98*, pp 610–616, John Wiley & Sons.
18. BURGREEN, G.W. Three-Dimensional Aerodynamic Shape Optimization using Discrete Sensitivity Analysis, May 1994, PhD dissertation, Dept of Mechanical Engineering, Old Dominion Univ, Norfolk, VA, USA.
19. BURGREEN, G.W. and BAYSAL, O. Three-dimensional aerodynamic shape optimization using discrete sensitivity analysis, *AIAA J*, September 1996, **34**, (9), pp 1761–1770.
20. LE MOIGNE, A. A Discrete Navier-Stokes Adjoint Method for Aerodynamic Optimisation of Blended Wing-Body Configurations, 2002, PhD dissertation, College of Aeronautics, Cranfield Univ, Cranfield, UK, available at http: //hdl.handle.net/1826/826.
21. LE MOIGNE, A. and QIN, N. Variable-fidelity aerodynamic optimization for turbulent flows using a discrete adjoint formulation, *AIAA J*, July 2004, **42**, (7), pp 1281–1292.
22. WAKAYAMA, S. Multidisciplinary design optimization of the blended-wing-body, 1998, Seventh AIAA/USAF/NASA/ISSMO symposium on multidisciplinary analysis and optimization, St Louis, MO, 2-4 September 1998, **3**, pp 1771–1779, AIAA–98–4938.
23. WAKAYAMA, S. Blended-wing-body optimization problem setup, September 2000, AIAA Paper 2000-4740.
24. GILMORE, R., WAKAYAMA, S. and ROMAN, D. Optimization of high-subsonic blended-wing-body configurations, September 2002, AIAA Paper 2002-5666.
25. MIALON, B., FOL, T. and BONNAUD, C. Aerodynamic optimization of subsonic flying wing configurations, June 2002, AIAA Paper 2002-2931.
26. HACKETT, K.C. and GIBSON, T. Aerodynamic studies of novel high speed configurations in the NEXUS programme, 2005, CEAS/KATnet Conference on Key Aerodynamic Technologies, Bremen, Germany, 20-22 June 2005.
27. ALEXANDROV, N.M., LEWIS, R.M., GUMBERT, C.R., GREEN, L.L. and NEWMAN, P.A. Optimization with variable-fidelity models applied to wing design, January 2000, AIAA Paper 2000-0841.

https://doi.org/10.1017/S0001924000001457 Published online by Cambridge University Press

28. ALEXANDROV, N.M., NIELSEN, E.J., LEWIS, R.M. and ANDERSON, W.K. First-order model management with variable-fidelity physics applied to multi-element airfoil optimization, 2000, Eighth AIAA/USAF/NASA/ISSMO Symposium on Multidisciplinary Analysis and Optimization, September 2000, AIAA Paper 2000-4886.
29. ALEXANDROV, N.M., LEWIS, R.M., GUMBERT, C.R., GREEN, L.L. and NEWMAN, P.A. Approximation and model management in aerodynamic optimization with variable-fidelity models, *J Aircr*, November-December 2001, **38**, (6), pp 1093–1101.
30. QIN, N. Aerodynamic studies for blended wing body aircraft, September 2002, AIAA Paper 2002-5448.
31. QIN, N., VAVALLE, A. and LE MOIGNE, A. Spanwise lift distribution for blended wing body aircraft, *J Aircr*, March-April 2005, **42**, (2), pp 356–365.
32. QIN, N., VAVALLE, A., LE MOIGNE, A., LABAN, M., HACKETT, K. and WEINERFELT, P. Aerodynamic considerations of blended wing body aircraft, *Progress in Aerospace Sciences*, August 2004, **40**, (6), pp 321–343.
33. SMITH, H. and YARF-ABBASI, A. *The MOB Blended Body Reference Aircraft*, November 2000, MOB Project Technical Report MOB/4/CU/TReport/No4.
34. OSHER, S. and SOLOMON, F. Upwind difference schemes for hyperbolic systems of conservation laws, *Mathematics of Computation*, April 1982, **38**, (158), pp 339–374.
35. CHAKRAVARTHY, S.R. and OSHER, S. Numerical experiments with the Osher upwind scheme for the Euler equations, *AIAA J*, September 1983, **21**, (9), pp 1241–1248.
36. VAN LEER, B. Towards the ultimate conservative difference scheme. III – upstream-centered finite-difference schemes for ideal compressible flow. IV – a new approach to numerical convection, *J Computational Physics*, March 1977, **23**, pp 263–299.
37. VAN LEER, B. Towards the ultimate conservative difference scheme. V – a second-order sequel to Godunov's method (for ideal compressible flow), *J Computational Physics*, July 1979, **32**, pp 101–136.
38. BALDWIN, B.S. and LOMAX, H. Thin layer approximation and algebraic model for separated turbulent flows, January 1978, AIAA Paper 78-257.
39. QIN, N., LUDLOW, D.K. and SHAW, S.T. A matrix-free preconditioned Newton/GMRES method for Navier-Stokes solutions, *Int J for Numerical Methods in Fluids*, June 2000, **33**, (3), pp 223–248.
40. SPEKREIJSE, S.P. Multigrid Solution of the Steady Euler Equations, 1987, PhD dissertation, Centrum Voor Wiskunde en Informatica, Amsterdam.
41. SHAW, S.T. Numerical Study of the Unsteady Aerodynamics of Helicopter Rotor Aerofoils, 1999, PhD dissertation, College of Aeronautics, Cranfield Univ, Cranfield, UK.
42. KORIVI, V.M., TAYLOR, A.C., NEWMAN, P.A., HOU, G.J.-W. and JONES, H.E. An approximately factored incremental strategy for calculating consistent discrete aerodynamic sensitivity derivatives, *J Computational Physics*, 1994, **113**, pp 336-346.
43. SHERMAN, L.L., TAYLOR, A.C., GREEN, L.L., NEWMAN, P.A., HOU, G.J.-W. and KORIVI, V.M. First- and second-order aerodynamic sensitivity derivatives via automatic differentiation with incremental iterative methods, *J Computational Physics*, 1996, **129**, (2), pp 307-331.
44. NEWMAN, P.A., HOU, G.J.-W., JONES, H.E., TAYLOR, A.C. and KORIVI, V.M. Observations on computational methodologies for uses in large-scale, gradient-based, multidisciplinary design, 1992, Fourth AIAA/USAF/NASA/OAI Symposium on Multidisciplinary Analysis and Optimization, 1992, **1**, pp 531-542.
45. VANDERPLAATS, G.N. *Numerical Optimization Techniques for Engineering Design: with Applications*, 1984, McGraw-Hill Book Company, New York.
46. GILL, P.E., MURRAY, W. and WRIGHT, M.H. *Practical Optimization*, 1981, Academic Press, London.
47. ZHOU, J.L., TITS, A.L. and LAWRENCE, C.T. *User's Guide for FFSQP Version 3.7: a FORTRAN Code for Solving Constrained Nonlinear (Minimax) Optimization Problems, Generating Iterates Satisfying all Inequality and Linear Constraints*, 1997, Systems Research Center TR-92-107r2, University of Maryland.
48. SCHMITT, V. and CHARPIN, F. Pressure distributions on the ONERA-M6-wing at transonic Mach numbers, 1979, Experimental Data Base for Computer Program Assessment, AGARD-AR-138, AGARD, Neuilly-sur-Seine, France.
49. SUNG, C. and KWON, J.H. Aerodynamic design optimization using the Navier-Stokes and adjoint equations, January 2001, AIAA Paper 2001-0266.
50. LEE, B.J., KIM, C.S., KIM, C., RHO, O.-H. and LEE, K.D. Parallelized design optimization for transonic wings using aerodynamic sensitivity analysis, January 2002, AIAA Paper 2002-0264.
51. KIM, H.-J. and NAKAHASHI, K. Discrete adjoint method for unstructured Navier-Stokes solver, January 2005, AIAA Paper 2005-449.
52. LABAN, M. Private communication.

https://doi.org/10.1017/S0001924000001457 Published online by Cambridge University Press